

Modeling of Long-Range Intra- and Inter-Species Charged Particle Collisions for PIC Simulations

D. D'Andrea^{1,*}, C.-D. Munz² and R. Schneider³

¹ *Forschungszentrum Karlsruhe - in der Helmholtz-Gemeinschaft, Institut für Kern- und Energietechnik, PF 3640, D-76021 Karlsruhe, Germany.*

² *Institut für Aerodynamik und Gasdynamik, Universität Stuttgart, Pfaffenwaldring 21, D-70550 Stuttgart, Germany.*

³ *Forschungszentrum Karlsruhe - in der Helmholtz-Gemeinschaft, Institut für Hochleistungsimpuls und Mikrowellentechnik, PF 3640, D-76021 Karlsruhe, Germany.*

Received 26 May 2009; Accepted (in revised version) 5 October 2009

Communicated by Xueqiao Xu

Available online 6 January 2010

Abstract. In this paper we present the modelling of elastic intra-species electron-electron and inter-species electron-ion scattering in a plasma on the basis of the Fokker-Planck collision operator. Taking into account the equivalence of this operator with a stochastic differential equation, we propose a Particle-in-Cell based approach for the numerical solution of the Fokker-Planck collision term. As we will see, the introduced numerical concept allows the simulation of the collisional relaxation process in a fully self-consistent fashion.

PACS: 52.20.Fs, 52.27.Aj, 52.65.Ff, 52.65.Rr

Key words: Coulomb collisions in plasmas, collisional relaxation, Fokker-Planck equation, stochastic differential equation, particle-in-cell method.

1 Introduction

A better physical understanding of electrical space propulsion systems like pulsed plasma thrusters [1] as well as a multitude of other discharge driven systems, in general, requires the numerical modelling and simulation of highly rarefied plasma flows. Mathematically, such phenomena demand a kinetic description which is established by the Boltzmann equation. An attractive numerical approach to tackle the non-linear Boltzmann problem consists in a combination of the well-known Particle-in-Cell (PIC) and Monte Carlo

*Corresponding author. *Email addresses:* danilo.dandrea@iket.fzk.de (D. D'Andrea), munz@iag.uni-stuttgart.de (C.-D. Munz), rudolf.schneider@ihm.fzk.de (R. Schneider)

methods. Basically, the minimal numerical model should accommodate the physics of interaction of charged particles with electromagnetic fields, elastic and inelastic electron-neutral scattering as well as elastic intra- and inter-species charged particle Coulomb collisions. Note, that the endeavor to include plasma particle interactions into fully kinetic simulations, usually carried out with PIC codes, have a long history (for a review see [2]).

In the present paper we focus our attention on elastic intra-species electron-electron and inter-species electron-ion collisions. For the plasmas of interest it is assumed that especially electron-electron interactions play a dominant role. They are crucial in determining the shape of the electron energy distribution function and are responsible for populating the high-energy tail of the velocity distribution to meet finally a Maxwellian distribution function. It is clear from energetic considerations that the high-energy part of the velocity distribution controls reactions like atomic excitation and ionization — the energy sinks for electrons — and to some extent the plasma chemistry. Furthermore, in bounded plasmas high-energy electrons can escape to the wall and thus establish an additional contest between depopulating and population the high-energy tail of the distribution function. Due to the long-range nature of the Coulomb force electron-electron collision is a result of a multiple small-angle scattering process of point charges. Besides inadmissible small time steps which are needed to resolve the individual collision event, electron-electron scattering is not a pure two-body interaction in a plasma because a single electron typically influences many other electrons at the same time. Hence, classical Monte Carlo (MC) tools like hard sphere models for (two-body) short-range reactions [3] seemed to be inadequate. Nevertheless several researchers successfully adapt binary collision models for long-range Coulomb interaction in a plasma, e.g. in a pioneer work Takizuka & Abé [4] proposed a (nonlinear) MC collision operator for PIC models which mimics the Fokker-Planck (FP) operator in Landau form. Later on Ma et al. [5] extended the Takizuka & Abé method for gyrokinetic simulations, where the scattering angle of a binary collision event obeys a Gaussian distribution. For this purpose they suggested a velocity-independent version of the Takizuka & Abé technique which relies on the local thermal velocity. Moreover, these authors introduced a fast and highly efficient implementation scheme for binary collisions. Afterwards, Wang and colleagues [6] improved the Takizuka & Abé ansatz. In particular, they clarified the relation between the newly proposed collision operator and the Landau operator which is equivalent to the FP collision term. Note, that all these authors attempted to show the consistency of their approach with the FP equation. However, none of these methods are derived from the FP collision operator. Definitely noteworthy is the cumulative small-angle scattering approach for the simulation of long-range Coulombs collisions introduced by Nanbu [7]. This approach represents a MC method which was deviated on the basis of physical considerations and do not use any kinetic equation. Although it was shown in [8] that this method is compatible with a first order solution of the Boltzmann equation (in Landau form) in Δt , this cumulative small-angle approach as well as the other mentioned methods are non self-consistent techniques to simulate the evolution of the distribution func-

tion due to charged particle interaction.

A promising alternative to the mentioned techniques is to represent elastic intra- and inter-species charged particle Coulomb collisions through a Fokker-Planck equation. In the PIC community first Jones and coworkers [9] used the equivalence of the FP with a Langevin equation and modeled isotropic electron-electron scattering by a grid-based "collisional field" and a velocity-independent constant collision frequency. However, this approach is only applicable when the distribution function is close to Maxwellian. Later on Manheimer et al. [10] improved the approach of Jones and coworkers by introducing a Langevin formulation, where the velocity-dependent friction force vector and the diffusion tensor are obtained from the distribution function of the scattering population which is assumed to be isotropic.

In the present paper we tie up to the proceeding of Manheimer and colleagues and start from the FP equation to describe elastic electron-electron and electron-ion collisions in a plasma. The keys to compute the friction force vector and the diffusion tensor are the Rosenbluth potentials. However, in order to circumvent any model assumptions like isotropic velocity distribution of the field particles in computing these potentials, we observe that they are given by convolution integrals which addresses to use Fourier transform techniques to calculate these quantities and their derivatives. Finally, the combination of a Langevin-type stochastic differential equation together with Fourier techniques and appropriate particle-mesh methods, allows a first principle, full self-consistent simulation of the collisional relaxation process.

To outline this PIC-based approach for the numerical solution of the FP equation, we state in Section 2 the governing equations for charged particle collisions in a plasma. Afterwards in Section 3, the overall numerical framework is briefly sketched out together with the basic ideas and techniques to solve numerically the Langevin-type equation. Results obtained from numerical experiments for intra- and inter-species as well as coupled intra-inter-species scattering are presented in Section 4. Finally, a short summary and an outlook of our further activities are given in Section 5.

2 Mathematical model of Coulomb interaction in plasmas

In this section we focus our attention on a brief review of the basic equations necessary to model elastic intra-species electron-electron and inter-species electron-ion — abbreviated by (e,e) and (e,h), respectively — Coulomb scattering in a plasma.

2.1 Statement of the governing equations

To describe elastic intra- and inter-species charged particle Coulomb collisions in a plasma it is convenient to start from the the Fokker-Planck (FP) equation (see, for instance,

[11–13])

$$\left(\frac{\delta f_e}{\delta t}\right)_{\text{col}} = -\nabla_v \left[\mathbf{F}_e(\mathbf{v}, t) f_e \right] + \frac{1}{2} \nabla_v^T \left[\nabla_v^T \left(\mathbb{D}_e(\mathbf{v}, t) f_e \right) \right]^T, \quad (2.1)$$

where ∇_v denotes the usual differential operator with respect to velocity \mathbf{v} . This equation describes the evolution of the electron distribution function $f_e = f_e(\mathbf{v}, t)$ — in which we are interested here — as a result of multiple small-angle Coulomb scattering of point charges, and represents the lowest order approximation to the Boltzmann collision integral. Therefore, it is not amazing that the FP model retains the significant properties of the Boltzmann integral [14, 15]. Furthermore, note that the occurrence of the FP equation for the description of elastic charged particle collisions in a plasma indicates that the short-time behavior of the transition probability is modeled as a diffusion process (see [16]). Basic for the present paper is the fact that the FP equation (2.1) is entirely equivalent to a stochastic differential equation (SDE). This means that the stochastic variable $\mathbf{V} = \mathbf{V}(t)$ — identified later with the velocity of the electrons — with transition density f_e fulfills the equation (also called Langevin-type equation in the following)

$$d\mathbf{V}(t) = \mathbf{F}_e(\mathbf{V}, t) dt + \mathbb{B}_e(\mathbf{V}, t) d\mathbf{W}(t), \quad (2.2)$$

where $\mathbf{W}(t) \in \mathbb{R}^3$ represents the three-dimensional Wiener process and the matrix $\mathbb{B}_e \in \mathbb{R}^{3 \times 3}$ is related to $\mathbb{D}_e \in \mathbb{R}^{3 \times 3}$ according to $\mathbb{D}_e = \mathbb{B}_e \mathbb{B}_e^T$. For sophisticated details and stringent proofs we address the reader to references [16, 17] and also to [18].

2.1.1 Intra-species (e,e)-collisions

In the latter equations, (2.1) and (2.2), the central quantities are the dynamical friction force (or drift) vector $\mathbf{F}_e = \mathbf{F}_e(\mathbf{v}, t) \in \mathbb{R}^3$ and the diffusion tensor $\mathbb{D}_e = \mathbb{D}_e(\mathbf{v}, t)$. Both, in general, depend also on the actual location \mathbf{x} which is not taken into account in the following. Their components are defined by

$$F_{e,j} = \sum_s n_s \Gamma_P^{(es)} \left(1 + \frac{m_e}{m_s} \right) \frac{\partial \mathcal{H}_s}{\partial v_j} \quad (2.3)$$

and

$$D_{e,jk} = \sum_s n_s \Gamma_P^{(es)} \frac{\partial^2 \mathcal{G}_s}{\partial v_j \partial v_k}, \quad (2.4)$$

respectively, where the index "s" goes over all scattering populations (sometimes called the field particles) with charge q_s , mass m_s , density n_s and temperature T_s , which are the electron or/and ion populations in the present context. Here,

$$\Gamma_P^{(es)} = \frac{e^2 q_s^2}{4\pi \epsilon_0^2 m_e^2} \ln(\Lambda)$$

denotes the plasma parameter (see [19]), where ϵ_0 is the permittivity of free space and $\ln(\Lambda)$ is the Coulomb logarithm in the classical limit. Note that the quantity $\bar{v}_{es} = n_s \Gamma_P^{(es)} / \bar{v}_s^3$

can be considered as an energy-weighted average of the speed-dependent momentum transfer collision frequency between the electrons "e" and the species "s", where the thermal velocity is given by $\bar{v}_s^2 = k_B T_s / m_s$ with the Boltzmann constant k_B . The keys to compute friction force and diffusion coefficients are the Rosenbluth potentials [11] which are defined by

$$\mathcal{H}_s(\mathbf{v}, t) = \int_{\mathbb{R}^3} d^3w \frac{f_s(\mathbf{w}, t)}{|\mathbf{g}|}, \quad \mathcal{G}_s(\mathbf{v}, t) = \int_{\mathbb{R}^3} d^3w |\mathbf{g}| f_s(\mathbf{w}, t), \quad (2.5)$$

where $\mathbf{g} = \mathbf{v} - \mathbf{w}$ is the difference between the velocity \mathbf{v} of the scattered-off (also called test) particles and the velocity \mathbf{w} of the field particles. Clearly, the drift vector \mathbf{F}_e and the diffusion tensor \mathbb{D}_e as well as the derived — "square root" — tensor \mathbb{B}_e themselves depend on the velocity \mathbf{v} and, hence, both Eqs. (2.1) and (2.2) are, in general, non-linear problems which have to be solved numerically in an appropriate manner. The direct numerical solution of the FP equation can be performed (see, for instance [20] and references given therein), but such an approach will make no clear link to the available PIC-based numerical tools for computing the particle distribution function in phase space [21]. A more promising approach is established by the use of the SDE (2.2) to which we will turn our attention in the next section. There, we also present the numerical methods that allow to compute the Rosenbluth potentials and their derivatives, especially for elastic intra-species scattering without any assumptions.

2.1.2 Inter-species (e,h) collisions

In the situation of intra-species (e,e) scattering a priori no knowledge about the velocity of field electrons after collision is available. However, in the case of inter-species (e,h) collisions plausible estimations are obvious. Here, we exploit the fact that the velocity of the electrons $v = |\mathbf{v}|$ is much larger than the one of the ions $w = |\mathbf{w}|$ and, furthermore, the smallness of their mass ratio is taken into account. Then, it is appropriate to perform a Taylor expansion of $|\mathbf{g}|^{-1}$ and $|\mathbf{g}|$ up to lowest order to obtain the approximated Rosenbluth potentials which take the simple form

$$\mathcal{H}_h(\mathbf{v}, t) = \frac{1}{v} - \frac{3\bar{v}_h^2}{4v^3} \quad \text{and} \quad \mathcal{G}_h(\mathbf{v}, t) = v + \frac{3\bar{v}_h^2}{4v}, \quad (2.6)$$

where it is assumed that $f_h(\mathbf{w}, t)$ is normalized in velocity space and that the mean $\int_{\mathbb{R}^3} d^3w \mathbf{w} f_h$ vanishes. From these results we immediately obtain the friction force vector

$$\mathbf{F}_e(\mathbf{v}, t) = -n_h \Gamma_P^{(eh)} v^{-2} \left(1 - \frac{9\bar{v}_h^2}{4v^2} \right) \hat{\mathbf{v}} \quad (2.7)$$

and the diffusion tensor

$$\mathbb{D}_e(\mathbf{v}, t) = n_h \Gamma_P^{(eh)} v^{-1} \left[\mathbb{H} - \frac{3\bar{v}_h^2}{4v^2} \left(\mathbb{I} - 3\hat{\mathbf{v}}\hat{\mathbf{v}}^T \right) \right] \quad (2.8)$$

with

$$\mathbb{H} = \mathbb{I} - \hat{\mathbf{v}}\hat{\mathbf{v}}^T, \quad (2.9)$$

where the unit vector $\hat{\mathbf{v}} = (\hat{v}_1, \hat{v}_2, \hat{v}_3)^T = \mathbf{v}/v$ is introduced for the sake of convenience.

In the following we examine the situation $\bar{v}_h^2/v^2 \ll 1$ in detail (see also [10]) and note first that in this case \mathbb{D}_e represents the transversal diffusion since $\hat{\mathbf{v}}^T \mathbb{H} = 0$. Second, due to the special properties of the matrix (2.9) namely, $\mathbb{H}^T = \mathbb{H}$ and $\mathbb{H}^T \mathbb{H} = \mathbb{H}$ we conclude that the square root tensor \mathbb{B}_e can be written immediately as

$$\mathbb{B}_e = \alpha v \mathbb{H} \quad (2.10)$$

with the abbreviation $\alpha^2 = n_h \Gamma_p^{(eh)} v^{-3}$. Note, that in contrast to the diffusion matrix defined by (2.8) as well as the situation of intra-species collisions no eigenvalue problem has to be solved to obtain \mathbb{B}_e for the present approximation. Assuming that the energy of the electrons is conserved exactly, i.e. $v = |\mathbf{v}| = \text{constant}$ and identifying $\hat{\mathbf{v}}$ with $\hat{\mathbf{V}}$, the SDE (2.2) takes the form

$$d\hat{\mathbf{V}}(t) = -\alpha^2 \hat{\mathbf{V}}(t) dt + \alpha \mathbb{H} d\mathbf{W}(t) \quad (2.11)$$

which establishes an equation for the sines and cosines of the polar and azimuthal angles. Since the matrix \mathbb{H} is not linear in $\hat{\mathbf{v}}$ an exact solution of Eq. (2.11) is not expected. However, taking into account the zero expectation property of the Itô integral and using the Itô formula (see Section 3.2) [16, 17] it is possible to find ordinary differential equations for both the mean and second moment. The solution of these equation are directly given by

$$M_i(t) = e^{-\alpha^2(t-t_0)} M_i(t_0) \quad (2.12)$$

and

$$P_{ij}(t) = 1/3 \delta_{ij} + \left[P_{ij}(t_0) - 1/3 \delta_{ij} \right] e^{-3\alpha^2(t-t_0)}, \quad (2.13)$$

where δ_{ij} denotes the Kronecker symbol, $M_i(t)$ and $P_{ij}(t)$, $i, j = 1, 2, 3$, are the elements of the expectation values $\mathcal{E}\{\hat{\mathbf{V}}\}$ and $\mathcal{E}\{\hat{\mathbf{V}}\hat{\mathbf{V}}^T\}$, respectively, and t_0 is the initial time (see also [22]). It is obvious, that the higher the electron velocity the slower the final moments (2.12) and (2.13) are reached. In essence, the consequence of the performed approximation in the inter-species (e,h) collision case is that the evolution of the electron and ion distribution function is decoupled. That means, the force experienced by the electron in a collision with an ion depends on its own velocity — especially only, if the leading term of the right-hand side of (2.7) and (2.8) is considered — and on the (higher) moments of the ion distribution function, which clearly differs from the intra-species collisional relaxation process. In addition, the cumulative effects of impacts cannot thermalize the electrons because they cannot change their velocity but only their direction.

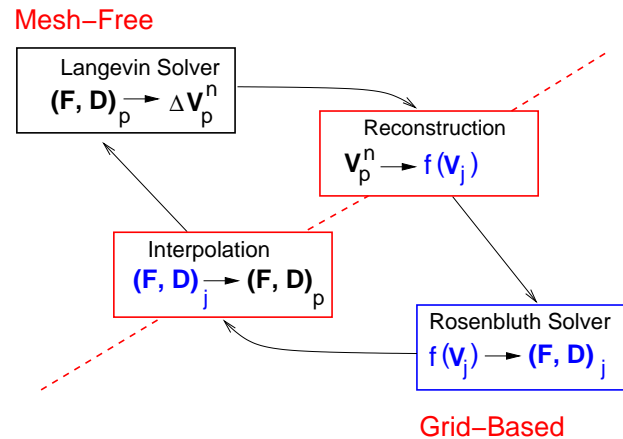


Figure 1: Building blocks of the PIC-based approach for the Fokker-Planck equation.

3 Numerical framework

In this section we briefly outline the PIC-based concept for the numerical solution of the FP equation, where especially the equivalence of this equation with the SDE (2.2) is exploited. The entirety of these techniques allow to compute the collisional relaxation process in a fully self-consistent way.

3.1 The PIC approach for the FP equation

Here, the PIC-based approach to solve the FP equation numerically is reviewed shortly (for details see [23]); more information of the general PIC methodology can be found in the books of Hockney & Eastwood [24] and Birdsall & Langdon [25]. For sake of clearness, we consider in the following a single spatial grid cell, in which a sufficiently large number of particles is located, and assume that a computational Cartesian mesh in velocity space is associated with this local grid zone. From Fig. 1 the analogy with the classical PIC concept is immediately evident: One part of the computational cycle is situated in a mesh-free zone, while another one needs a discretization grid, with two interface procedures closing the whole calculation. In the following, a short description of the single building blocks of the Fokker-Planck solver is given.

Reconstruction. From the actual location of the plasma particles in the three-dimensional mesh-free velocity space, the distribution function $f_e(\mathbf{v}, t)$ is resolved on the Cartesian velocity mesh with equidistant spacing. It is well-known that for such mesh arrangements simple and very effective localization strategies are available. Furthermore, we apply the volume-weighting technique — the straightforward extension of the area-weighting method — to compute relative coordinates for each particle with index “ v ” from which individual particle weights $w^{(v)}$ can be determined (see Appendix A). These particle weights then contain the necessary information to assign each particle to the eight nodes

of the corresponding grid cell of the velocity mesh and to reconstruct the distribution function needed for the next section.

Rosenbluth Solver. The assumption of an isotropic but non-Maxwellian velocity distribution of the scatterer implies an enormous reduction of the problem since the diffusion and friction coefficients can be written in terms of one-dimensional quadratures [10, 13, 26]. However, in cases where no model assumptions concerning the distribution function can be imposed, it seemed to be expedient to apply Fourier transformation techniques [27, 28] to evaluate the Rosenbluth potentials (2.5) and also their derivatives, because they are convolutions of the scatterer distribution function and of the absolute value of the relative velocity. In this context it is worth mentioning that the use of the analytical Fourier transform of g^{-1} increase the efficiency of the computations. Furthermore, bear in mind that the application of the Fourier approach allows a first principle determination of the deterministic friction and stochastic diffusion arising in the SDE (2.2) which results in the self-consistent modeling of collisional relaxation. Note, that in classical PIC methods for the Vlasov equation a Poisson or Maxwell solver undertakes the task of the Rosenbluth solver.

Interpolation. The "Langevin forces", which are the deterministic friction and the stochastic diffusion (as well as the square root of the diffusion), have to be computed at the actual position of each particle in grid-free velocity space. Since interpolation is nothing else than the "inverse operation" of assignment, the particle weights $w^{(v)}$ are once again used to interpolate the Langevin forces at the location of particle "v" in continuous velocity space (see Appendix A).

Langevin Solver. Under the action of the velocity-dependent Langevin forces, each particle is moved in velocity space according to the Langevin-type equation (2.2), where appropriate numerical methods are required. For our purposes, we use weak approximations to the SDE (2.2). Note, that the SDE takes the role of the deterministic Lorentz equation in the classical PIC approach.

3.2 Numerical solution of the Langevin-type equation

The mathematical character of the SDE (2.2) contrasts sharply with its deterministic counterpart. Especially, this fundamental difference finds expression in the numerical approximation of the stochastic law of dynamics (2.2). In the following, we sketch out in short the path of approximation for the SDE and start from its equivalent stochastic integral formulation

$$\mathbf{V}(t) = \mathbf{V}(t_0) + \int_{t_0}^t \mathbf{F}\{s\} ds + \sum_{p=1}^3 \int_{t_0}^t \mathbf{b}_p\{s\} dW^p(s), \quad (3.1)$$

where the subscript "e" has been omitted for convenience. Here, the column vector $\mathbf{b}_p = \mathbb{B}\mathbf{e}_p$ with the usual Cartesian unit vectors $\mathbf{e}_p \in \mathbb{R}^3$ is introduced, $\{s\}$ abbreviates $(\mathbf{V}(s), s)$

and $t = t_0 + \Delta t$. Note, that the first integral on the right-hand side of (3.1) is an ordinary integral (of Riemann or Lebesgue type) while the second one is a stochastic integral — here — in the Itô sense with peculiar calculus and properties (see, for instance [16, 17, 29]). In order to obtain an appropriate weak numerical scheme to solve (3.1) we use the integrated form of the multi-dimensional Itô formula,

$$\Psi\{t\} = \Psi\{t_0\} + \int_{t_0}^t ds \left[\mathcal{L}^{(0)}\Psi \right]\{s\} + \sum_{p=1}^3 \int_{t_0}^t dW^p(s) \left[\vec{b}_p \cdot \nabla_c \Psi \right]\{s\} \tag{3.2}$$

for the arbitrary function Ψ , where the diffusion operator $\mathcal{L}^{(0)}$ is defined by

$$\mathcal{L}^{(0)}\Psi = \left\{ \frac{\partial}{\partial t} + \sum_{j=1}^3 F_j \frac{\partial}{\partial v_j} + \frac{1}{2} \sum_{j,k=1}^3 D_{jk} \frac{\partial^2}{\partial v_j \partial v_k} \right\} \Psi.$$

Applying (3.2) recursively to the components of the friction vector $\Psi = F_j$ and the square root tensor $\Psi = B_{jk}$, respectively, we get the truncated weak Itô-Taylor expansion (ITE) for the stochastic variable \mathbf{V} . The desired order of weak convergence is closely related with the underlying hierarchical set of multi-indices, which itself determines the truncation of the Itô-Taylor series. Keeping in the following all stochastic integrals with multi-index μ of length $l(\mu) \leq 2$, one obtains the multi-dimensional — that is three spacial dimensions and three independent Wiener processes — second order weak ITE

$$\begin{aligned} \mathbf{V}(t_0 + \Delta t) = & \mathbf{V}(t_0) + \mathbf{F}\{t_0\} \mathcal{I}_{(0)} + \sum_{p=1}^3 \mathbf{b}_p\{t_0\} \mathcal{I}_{(p)} + \sum_{p,q=1}^3 \left[\mathbf{b}_p \cdot \nabla_v \mathbf{b}_q \right]\{t_0\} \mathcal{I}_{(p,q)} \\ & + \sum_{p=1}^3 \left[\mathbf{b}_p \cdot \nabla_v \mathbf{F} \right]\{t_0\} \mathcal{I}_{(p,0)} + \sum_{p=1}^3 \left[\mathcal{L}^{(0)} \mathbf{b}_p \right]\{t_0\} \mathcal{I}_{(0,p)} + \left[\mathcal{L}^{(0)} \mathbf{F} \right]\{t_0\} \mathcal{I}_{(0,0)}, \end{aligned} \tag{3.3}$$

where the occurring multiple Itô integrals are given by

$$\mathcal{I}_{(p)} = \int_{t_0}^{t_0 + \Delta t} dW^p(s) \quad \text{and} \quad \mathcal{I}_{(p,q)} = \int_{t_0}^{t_0 + \Delta t} dW^q(s_2) \int_{t_0}^{s_2} dW^p(s_1)$$

with the convention $dW^0(s) = ds$. For more details about the ITE we address the reader to the literature, for instance [17]. Moreover, we note that the first three terms on the right-hand side of (3.3) establish a first order weak scheme while the additional four terms are necessary to assure a second order weak series expansion. A characteristic feature of weak approximation is the freedom to replace multiple Itô integrals by suitable simpler random numbers which coincide with the lower order moments. Then, after the replacements of the Itô integrals by simpler noise increments, one obtains from the ITE (3.3) the desired — but still non-derivative free — order two weak Milstein scheme. It is clear from (3.3) that this weak expansion requires the evaluation of derivatives up to second order of the friction and derived diffusion coefficients. However, in the environment of self-consistent computations the drift and diffusion coefficients are not known analytically in the course of the simulation and, hence, it is desirable to avoid the use of such derivatives. To

obtain an explicit scheme, i.e. to avoid completely the differentiations in (3.3), one has to observe the occurrence of the Itô formula for the friction vector \mathbf{F} in the Milstein scheme and to shift the remaining derivatives with the aid of deterministic Taylor expansions (for details see, [23]). Then, for the discrete approximation \mathbf{V}_n of $\mathbf{V}(t_n)$ with $\mathbf{V}_0 = \mathbf{V}(t_0)$ the explicit order two weak Itô-Taylor scheme takes the form [17]

$$\begin{aligned} \mathbf{V}_{n+1} = & \mathbf{V}_n + \frac{\Delta t}{2} [\mathbf{F}(\mathbf{V}_{n+1}^*) + \mathbf{F}(\mathbf{V}_n)] + \frac{1}{4} \sum_{p=1}^3 \left\{ [\mathbf{b}_p(\mathbf{T}_p^+) + \mathbf{b}_p(\mathbf{T}_p^-) + 2\mathbf{b}_p(\mathbf{V}_n)] \Delta W_n^p \right. \\ & + \sum_{\substack{q=1 \\ q \neq p}}^3 [\mathbf{b}_p(\mathbf{U}_q^+) + \mathbf{b}_p(\mathbf{U}_q^-) - 2\mathbf{b}_p(\mathbf{V}_n)] \Delta W_n^p \left. \right\} + \frac{1}{4\sqrt{\Delta t}} \sum_{p=1}^3 \left\{ [\mathbf{b}_p(\mathbf{T}_p^+) \right. \\ & \left. - \mathbf{b}_p(\mathbf{T}_p^-)] [(\Delta W_n^p)^2 - \Delta t] + \sum_{\substack{q=1 \\ q \neq p}}^3 [\mathbf{b}_p(\mathbf{U}_q^+) - \mathbf{b}_p(\mathbf{U}_q^-)] [\Delta W_n^p \Delta W_n^q + R_n^{p,q}] \right\} \end{aligned} \quad (3.4)$$

with the auxiliary vectors

$$\mathbf{V}_{n+1}^* = \mathbf{V}_n + \mathbf{F}(\mathbf{V}_n) \Delta t + \sum_{p=1}^3 \mathbf{b}_p(\mathbf{V}_n) \Delta W_n^p, \quad (3.5)$$

$$\mathbf{T}_p^\pm = \mathbf{V}_n + \mathbf{F}(\mathbf{V}_n) \Delta t \pm \mathbf{b}_p(\mathbf{V}_n) \sqrt{\Delta t}, \quad (3.6)$$

$$\mathbf{U}_q^\pm = \mathbf{V}_n \pm \mathbf{b}_q(\mathbf{V}_n) \sqrt{\Delta t}, \quad (3.7)$$

and the time increment Δt , where it is assumed that the vector functions \mathbf{F} and \mathbf{b}_p do not depend explicitly on time. Here, ΔW_n^p is a Gaussian random number with mean $\mathcal{E}\{\Delta W_n^p\} = 0$ and variance $\mathcal{E}\{(\Delta W_n^p)^2\} = \Delta t$ which is compactly expressed by the notation $\Delta W_n^p \sim \mathcal{N}(0, \Delta t)$. The quantity $R_n^{p,q}$ is given by $R_n^{p,q} = -\Delta t$ for $p = q$ while for $p > q$ $R_n^{p,q} \sim \mathcal{N}(0, (\Delta t)^2)$ and $R_n^{q,p} = -R_n^{p,q}$, where $p, q = 1, 2, 3$. It should be pointed out, that the "predictor step" (3.5) represents nothing else than the explicit first order weak Euler — or Euler-Maruyama — scheme. Finally note, that recently a slightly modified weak second-order scheme has been proposed in [30] which is developed on the basis of the weakly convergence requirement and the sufficient moment conditions. Although this scheme is somewhat more efficient than the second order weak Milstein scheme it is also non-derivative free and, hence, we prefer the Itô-Taylor scheme (3.4) for our investigations.

To get an appreciation of the approximation characteristics of the introduced weak schemes, we consider the one-dimensional SDE

$$dV(t) = \beta V(t) dt + \gamma_1 V(t) dW^1(t) + \gamma_2 V(t) dW^2(t) \quad (3.8)$$

for the variable V which depend on t with two independent Wiener increments and initial value $V_0 = 3.0$, where $\beta = 1.5$ and $\gamma_1 = \gamma_2 = 0.02$. Note, all quantities appearing in the latter equation have no units. Clearly, applying Itô calculus, one immediately gets $M(t) = V_0 e^{\beta t}$

for the mean value. While solving the linear SDE (3.8) respectively, with the weak Euler (3.5) and the second order weak scheme (3.4) for the discretizations $\Delta t = 0.25$ and $\Delta t = 0.125$, we record the relative error

$$\epsilon_R(t) = \frac{1}{M(t)} |M(t) - \langle V(t) \rangle|,$$

where the sample average

$$\langle V(t) \rangle = \frac{1}{N_p} \sum_{v=1}^{N_p} V^{(v)}(t)$$

is computed for $N_p = 10^5$ simulation particles. The evolution of $\epsilon_R(t)$ obtained from the Euler and the second order weak scheme is seen in Fig. 2. Clearly, the relative error of the weak second order Itô-Taylor scheme for the coarsest discretization is always below that one of the Euler scheme for the smallest Δt . This means that the second order approach allows a calculation of the mean value with an accuracy which is never reached by the first order Euler method. The jagged behavior of the second order result for $\Delta t = 0.125$ seemed to be a hint that more simulation particles are needed for higher order computations with small discretization Δt . This speculation is affirmed by the thick line without symbols seen in Fig. 2, where 10^6 simulation particles are used. To determine the experimental order of convergence — that is also to demonstrate the consistency — of the schemes under consideration we plot in Fig. 3 $|M(T) - \langle V(T) \rangle|$ as a function of $\Delta t = 2^{-n}T$, $n = 1, 2, \dots$, in a double-log scale where $T = 1$. In addition to the results of the explicit first order Euler (line with full gradients) and the explicit second order weak scheme (line with full squares) we present in Fig. 3 the result obtained from the non-derivative free Milstein scheme (dashed-dotted lines with circles). From the slope of the first order Euler scheme we find a good agreement between design and experimental (~ 0.9) order of convergence. Similar, the behavior of the non-derivative free second order scheme is also very satisfactory and yields ~ 1.9 for the experimental convergence order. For large and moderate Δt ($2^{-1} \leq \Delta t \leq 2^{-4}$) the slope of the explicit scheme agrees very well with that of the weak Milstein scheme. However, for small step sizes ($\Delta t < 2^{-4}$) the second order explicit approach shows after a steeper slope a “plateau” behavior. A very similar behavior (not shown here) is also observed for the Milstein scheme, but for very small discretizations ($\Delta t < 2^{-7}$). The difference in the convergence behavior between second order explicit and Milstein scheme may be attributed to the additional approximation of the derivatives in the explicit case. The appearance of the “plateau” behavior is alleviated if the number of trajectories (that means simulation particles) considerably increases as already mentioned above.

4 Results

Each single block in Fig. 1 has been tested separately, thoroughly in its three-dimensional version [23] providing very good reliability. Here, we present the validation of

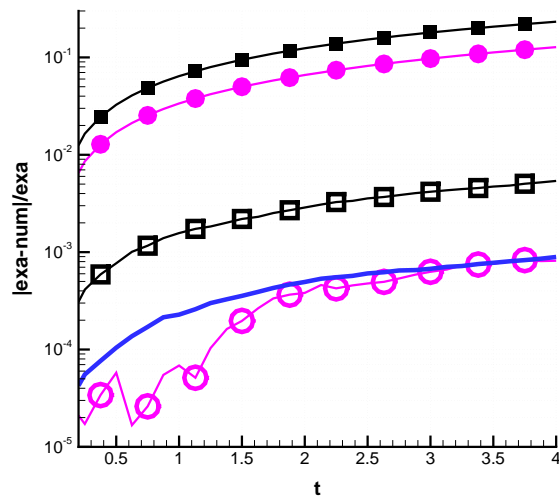


Figure 2: The evolution of the relative error between exact and numerical solution as a function of t , where a first order Euler (lines with full symbols) and a second order weak (lines with open symbols) scheme is applied with 10^5 simulation particles (squares: $\Delta t=0.25$; circles: $\Delta t=0.125$). The line without symbols represents the second order result for $\Delta t=0.125$ with 10^6 simulation particles.

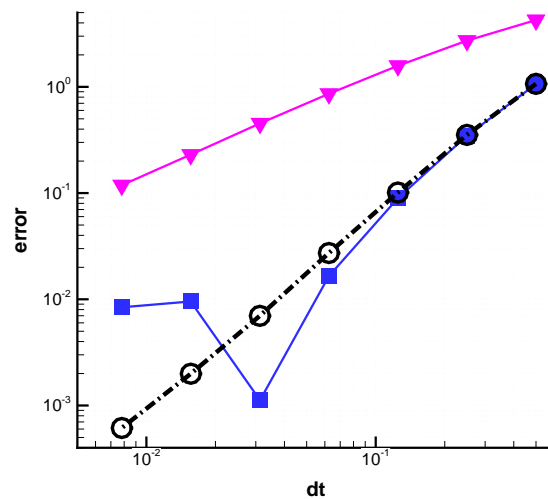


Figure 3: Log-log plot of the error versus the discretization Δt . First order Euler scheme: line with full gradients; second order explicit scheme: line with full squares and non-derivative free Milstein scheme: dashed-dotted line with circles.

the whole Fokker-Planck module by means of a sequence of numerical experiments for intra- and inter-species scattering demonstrating the good approximation properties of the introduced schemes. In order to perform a general investigation, all the quantities have been treated as dimensionless quantities. As reference sizes we considered the mass and charge of electrons with a number density of $n_c = 10^{18} \text{ m}^{-3}$. The thermal velocity \bar{v}_e

is derived from a Maxwellian distribution function of electrons at a temperature of $T_c = 10$ eV: $v_c = \bar{v}_e = 1.326 \cdot 10^6$ m/s. From these parameters and the plasma parameter $\Gamma_p^{(ee)}$ (see Section 2.1.1) one obtains that one time unit is equivalent to

$$t_c = v_c^3 / (n_c \Gamma_p^{(ee)}) = 0.22 \mu\text{s}.$$

4.1 Intra-species electron-electron Coulomb collisions

The first numerical experiment is designed for the validation and assessment of the applied approximation methods coded in the FP module. For this we consider the three dimensional normal distribution

$$f(\mathbf{v}) = (2\pi)^{-\frac{3}{2}} \prod_{i=1}^3 \frac{1}{\sigma_i} e^{-\frac{(v_i - \mu_i)^2}{2\sigma_i^2}}$$

which is also a solution of the FP equation (see, e.g., [12]). The numerical simulation is initialized as follows: In the mesh-free velocity space, the initial velocities components $V_i^{(\nu)}(t=0)$ of the $\nu = 1, \dots, N_p = 3 \cdot 10^5$ particles are independent identically distributed Gaussian random numbers with mean $\mu_i = 0$ and variance $\sigma_i^2 / v_c^2 = 4.0$ which also ensures that the velocity distribution is a Maxwellian. Subsequently, the PIC cycle (Fig. 1) with the weak second order Langevin solver (3.4) is $3 \cdot 10^3$ times passed through with time step size $\Delta t / t_c = 0.05$. Throughout this computation the velocity mesh which is needed for the Rosenbluth solver consists of $N_g = 64$ grid points in each direction. Since the system is in an equilibrium configuration, the shape of the velocity distributions as well as their variances, respectively depicted in Figs. 4 and 5, are not expected to change during the simulation. However, the latter shows a less satisfactory temporal behavior of the variance which in fact increases in time. This artificial warming — a measure for the lack of energy conservation [31] — is presumably due to the grid interface operations, especially, by the “particle sharing” of the nodes in the assignment procedure. The hypothesis that such a deviation from stationary solution is attributable to the grid is confirmed by the fact that the numerical solution is considerably improved by increasing the number of grid points, as clearly seen in Fig. 5 (line with triangles). The remaining increase in the variance may reflect the presence of other numerical errors — whereto also the effects of the finite sample size of the simulation particles belong to — which are inherent in any discrete approximation. To cure these insufficiencies we here revisited the normalization approach introduced by Lemons and coworkers [32] to provide global internal energy and mean velocity conservation. In the following this renormalization procedure is briefly recapitulated for sake of clarity and, in addition, a time-dependent extension is proposed. For this purpose we assume that the two conservation quantities, namely, the mean $\vec{\mu}_0 = \vec{\mu}(t_0)$ and the total variance $\sigma_0^2 = \sum_{i=1}^3 \sigma_i^2(t_0)$ are computed at the beginning of the simulation from the particles average. Furthermore, we require that the velocities $\mathbf{V}^{(\nu)}$, $\nu = 1, \dots, N_p$, of all simulation particles N_p are known at $t = t_n$ from the numerical

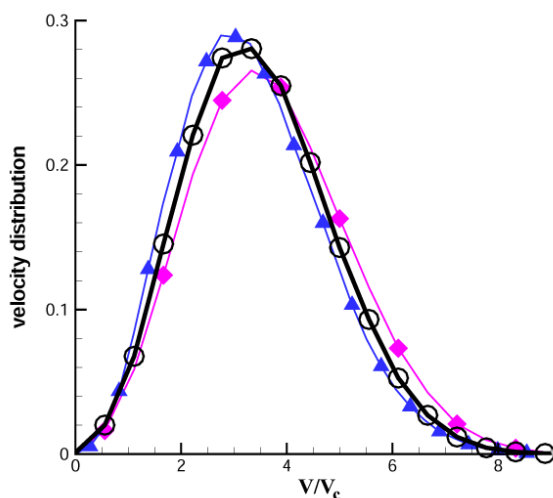


Figure 4: Distribution function recorded at $t/t_c = 150$. Full line: exact solution, line with full diamonds: 64^3 nodes, line with full triangles: 128^3 grid points. The numerical result obtained with 64^3 grid points and correction (open circles) coincides exactly with the analytical solution.

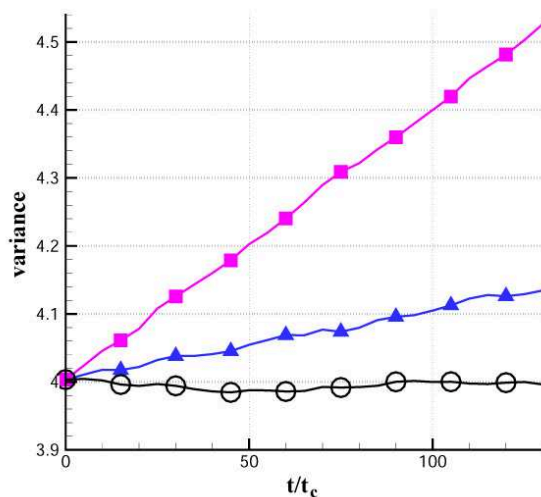


Figure 5: Comparison of the temporal evolution of the variance of the x -component for two discretizations of the Cartesian velocity mesh. Line with square: 64^3 grid points, line with triangles: 128^3 nodes, line with circles: 64^3 nodes and correction.

solution of the stochastic collision law (2.2). From this knowledge we then estimate the actual mean $\vec{\mu}_{ac}(t)$ and variance $\sigma_{ac}^2(t)$ according to

$$\mu_{ac,i} = \frac{1}{N_p} \sum_{v=1}^{N_p} V_i^{(v)} \quad \text{and} \quad \sigma_{ac,i}^2 = \frac{1}{N_p - 1} \sum_{v=1}^{N_p} (V_i^{(v)} - \mu_{ac,i})^2 \quad \text{for } i=1,2,3.$$

At each time step $t = t_n$, the internal energy of the whole system is given, essentially, by the sum of the variances in the three directions $\sigma_{ac}^2 = \sum_{i=1}^3 \sigma_{ac,i}^2(t)$ and is demanded not to change from σ_0^2 . From this requirement, a numerical error is evaluated as $\epsilon_N = \sigma_0^2 - \sigma_{ac}^2$ and in the spirit of the equipartition principle is equally subdivided in the three directions

$$\sigma_{de,i}^2 = \sigma_{ac,i}^2 - \frac{1}{3} \epsilon_N,$$

where $\sigma_{de,i}^2 = \sigma_{de,i}^2(t)$ denotes the "desired" value of the variances. In contrast to the variance, the desired mean value components $\mu_{de,i}$ are immediately obtained from $\mu_{de,i} = \mu_{0,i}$. Applying now the renormalization transformation according to

$$V_i^{(v)} \rightarrow \tilde{V}_i^{(v)} = \mu_{de,i} + \left(V_i^{(v)} - \mu_{ac,i} \right) \sqrt{\frac{\sigma_{de,i}^2}{\sigma_{ac,i}^2}} \tag{4.1}$$

one obtains the redistributed particle velocity function which ensures that the mean $\langle \tilde{V}_i \rangle = \mu_{de,i}$ and the variance $\sigma_{\tilde{V}}^2 = \sigma_{de,i}^2$ achieve the required values. In essence, the renormalization (4.1) eliminates any instabilizing fluctuations in the moments of the electron distribution f_e by linear transforming the particles velocities without changing the shape of the distribution functions so that their means and variances recover the desired values while the system evolves stochastically. Exactly this property is utilized to guarantee global energy and momentum conservation at each time step and its successful approach is clearly demonstrated by the results plotted additionally in the Figs. 4 and 5: The open circles lie exactly on the exact Maxwellian distribution (full thick line) and the variance (line with circles) stay — besides small oscillations — constant.

A further numerical experiment is performed to study the intra-species (e,e) relaxation of an arbitrary initial velocity distribution to its equilibrium from first principles. The velocity distributions of the $N_p = 3 \cdot 10^5$ simulation particles are initialized according to parabolas with different mean values ($\mu_x/v_c = 3.75$, $\mu_y/v_c = 3.0$ and $\mu_z/v_c = 2.25$) and variances ($\sigma_x^2/v_c^2 = 0.34$, $\sigma_y^2/v_c^2 = 0.59$ and $\sigma_z^2/v_c^2 = 0.94$) in each velocity direction. The evolution of these initial distributions is monitored for $2 \cdot 10^3$ iterations with time step size $\Delta t/t_c = 0.0125$, where the renormalization correction (4.1) is now applied. The first measurement of interest is seen in Fig. 6, where the temporal evolution of the three variances, computed from the particle velocities, are plotted. Since the diffusive intra-species collision model provides, by means of the friction and diffusion "forces", mechanisms that allow internal energy exchanges, one expects that such a system reaches thermal equilibrium. This expectation is clearly confirmed: During a transient phase ($t < 10$), where σ_z^2 (dashed-dotted line with diamonds) decays and σ_y^2 (dashed line with circles) slightly and σ_x^2 (full line with squares) strongly increase, the variances reach a common state after approximately 10^3 temporal cycles. The final configurations of the particle velocity distribution functions are depicted in Fig. 7. As a consequence of the properties of the FP approximation also a system of charged particles in a "naive" non-equilibrium condition

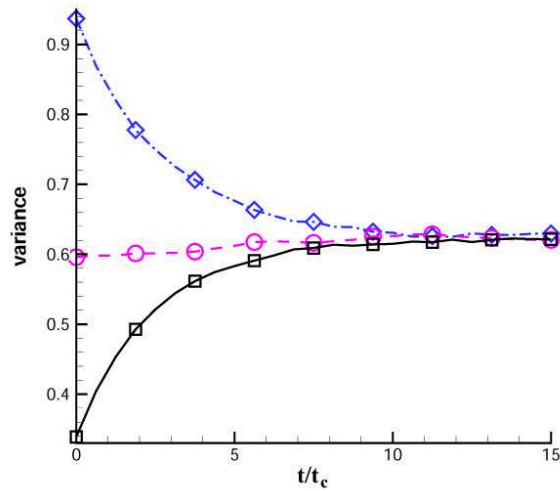


Figure 6: Temporal evolution of the variances ($\sigma_x^2(t)$ full line with squares, $\sigma_y^2(t)$ dashed line with circles and $\sigma_z^2(t)$ dashed-dotted line with diamonds) for the "parabola experiment".

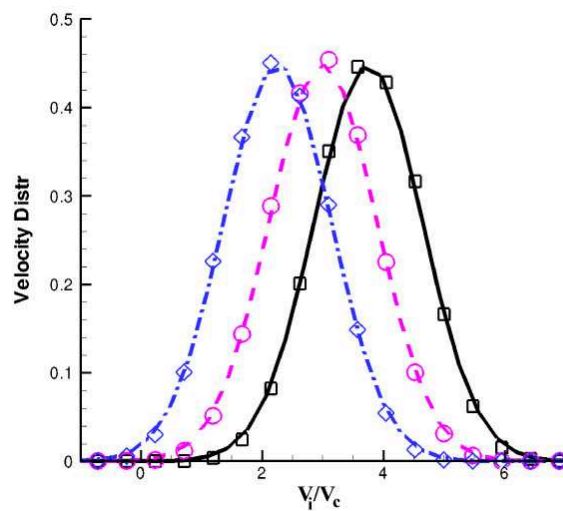


Figure 7: Final configuration of the particle velocity distribution functions (symbols) starting from the initial parabola data are compared with the exact expressions (lines) whose variances are obtained from Fig. 6.

evolves in the course of time to its equilibrium conditions, that is relaxes to Gaussian shaped distributions with same variance under positive entropy production. Note, the mean values of all velocity components remain constant since there is no external force to cause a stream motion of the particles.

For both numerical experiments presented above a velocity mesh was indispensable to reconstruct the velocity distribution function for the computation of the friction force and diffusion coefficients. Besides the numerical error due to the weak approximation

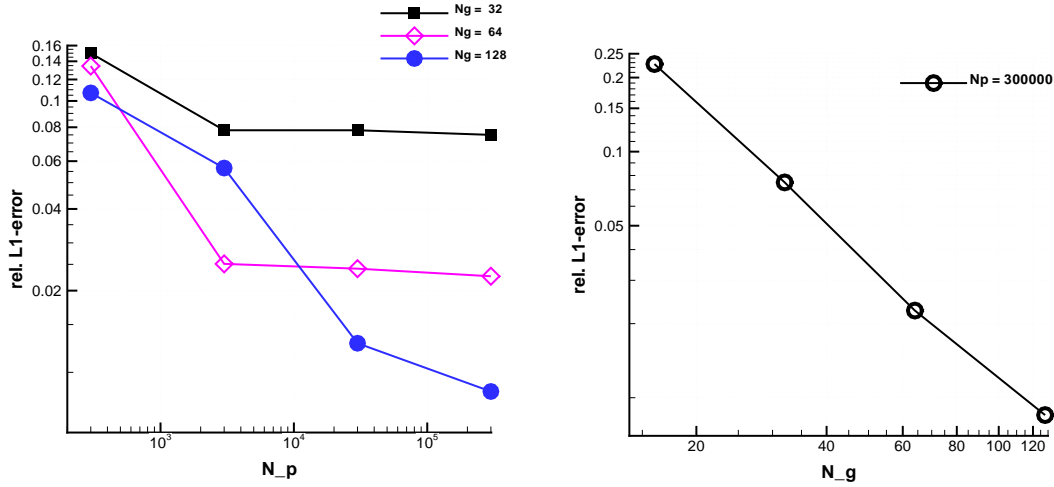


Figure 8: Left: Log-log plot of the L_1 -norm versus the number of simulation particles ($N_p = 3 \cdot 10^2, 3 \cdot 10^3, 3 \cdot 10^4, 3 \cdot 10^5$) for the discretization $N_g = 32$ (line with filled squares), $N_g = 64$ (line with open diamonds) and $N_g = 128$ (line with filled circles). Right: The averaged relative L_1 -norm of error as a function of the velocity mesh discretizations $N_g = 16, 32, 64$ and 128 .

of the SDE 2.2 (see Section 3.2), this proceeding clearly introduces additional numerical errors which are attributed to the particle-mesh and mesh-particle coupling as well as the grid computations (Fourier transformation, etc.) in the Rosenbluth solver. To judge the quality of the numerical method as a function of the number of particles N_p and the number of grid points N_g we calculate the physical quantity $Q(v) = \partial \mathcal{H}(v) / \partial v_x$ corresponding to the velocity dependent friction force in the v_x -direction and compare it with its exact value (see, e.g. [12]). This value is obtained by initializing the three directions of the velocity as three Gaussians: in the following we choose $\mu_i = 0$ and $\sigma_i^2 / v_c^2 = 1$. The comparison is done on $N_{pro} = 10^3$ “probe” positions which are uniformly distributed in the v_x -direction according to

$$U_{pro}^{(\lambda)} / v_c = 8(2Z - 1),$$

where $Z \in [0, 1]$ and $\lambda = 1, \dots, N_{pro}$. Starting, for instance, with $N_g = 32$ and varying N_p according to $3 \cdot 10^2, 3 \cdot 10^3, 3 \cdot 10^4$ and $3 \cdot 10^5$ it is possible to evaluate $Q(v)$ on the probes for each N_p and to construct a graph of the L_1 -norm of the distance from the exact reference solution as

$$\langle E_{L_1}(N_p, N_g) \rangle = \frac{1}{N_{pro}} \sum_{\lambda=1}^{N_{pro}} \frac{|Q_{num}(U_{pro}^{(\lambda)}; N_p, N_g) - Q_{ex}(U_{pro}^{(\lambda)})|}{|Q_{ex}(U_{pro}^{(\lambda)})|}. \tag{4.2}$$

If we repeat the same procedure for $N_g = 64$ and $N_g = 128$, respectively we finally obtain the left plot in Fig. 8. Initially increasing N_p decreases the error as intuitively expected but beyond a certain number of simulation particles ($N_g = 32, N_p \lesssim 10^3$; $N_g = 64, N_p > 10^3$ and $N_g = 128, N_p \geq 3 \cdot 10^5$) a sort of saturation effect arises. Actually when the distribution

function is sufficiently smooth a further increase of N_p can hardly improve the L_1 -norm of the error. The residual error seems to be a direct consequence of the applied assignment and interpolation (see Appendix A) which is formal second order accurate (see, e.g. [33]). To check this hypothesis we fixed the number of simulation particles in a spatial grid cell equal to $N_p = 3 \cdot 10^5$ — so that for the chosen N_g saturation is always met —, initialized the velocity of the particles as above and discretize the Cartesian velocity mesh by $N_g = 16, 32, 64, 128$ grid points in each direction resulting in a velocity step size of $\Delta v/v_c = 1.25, 0.6250, 0.3125, 0.1563$, respectively. The result of this numerical experiment is depicted in the right plot of Fig. 8, where the L_1 -error is shown as a function of the four discretizations N_g . Clearly, these errors are located nearly on a straight line. The absolute value of the slope of this line is a measure for the experimental order of convergence (EOC). We extract from the right curve of Fig. 8 an $\text{EOC} \sim 1.7$ which is a reasonable result since both the assignment and the interpolation procedure is second order accurate. Finally note, that in situations when the friction force and diffusion coefficients are given analytically (see next section) the coupling interfaces and the grid computations can be omitted and the discussed sources of error do not occur.

4.2 Simulation of inter-species Coulomb collisions

In this sub-section simulation results which allow the assessment of the inter-species collision model and module will be presented. For that purpose, we consider a monochromatic electron beam consisting of $3 \cdot 10^4$ simulation particles which enter the ions reservoir in x -direction $\hat{\mathbf{V}}(t_0) = (1, 0, 0)^T$ with initial velocity $|\mathbf{V}(t_0)|/v_c = 3$. The electrons are advanced according to the SDE (2.2) which is solved by an Euler scheme of kind (3.5), where the friction force is established by (2.7), the square root matrix \mathbb{B} is obtained from the diffusion tensor (2.8) by the solution of an eigenvalue problem [28] and the thermal velocity of the ions \bar{v}_h is fixed equal to $\bar{v}_e/48$. The event dynamics for $4 \cdot 10^3$ iterations is monitored through the electrons mean and variance seen in Fig. 9 together with their counterparts obtained from the exact moment equations (2.12) and (2.13). To guarantee the global conservation laws, the previously discussed renormalization technique (4.1) is applied, where the desired mean is now the actual one. Since (2.11) represents a stochastic law for the randomization of the directions in velocity space, we fixed σ_0^2 according to $\sigma_0^2 = \bar{\mu}^2(t_0)$. As reported in Fig. 9 (left), the electrons "loose" completely their initial drift velocity which is not noticed in the case of intra-species interaction. Obviously, the numerical result (open symbols) is nearly in perfect agreement with the exact solution (2.12) (full line); hardly visible deviations occur only for times greater than ~ 120 (which corresponds to $\sim 26 \mu\text{s}$). The initial kinetic energy is transformed in thermal energy which is redistributed in each direction according to the equipartition principle. This is observed in Fig. 9 (right), where the thermal evolution of $\sigma_x^2(t)$ (numerical: open squares; analytical: full line) and $\sigma_y^2(t)$ (numerical: open circles; analytical: dotted line) are plotted. Note, that also in this case a noteworthy concurrence between the numerical and exact result is observable. These variances show that the x -component of the electron velocity possesses

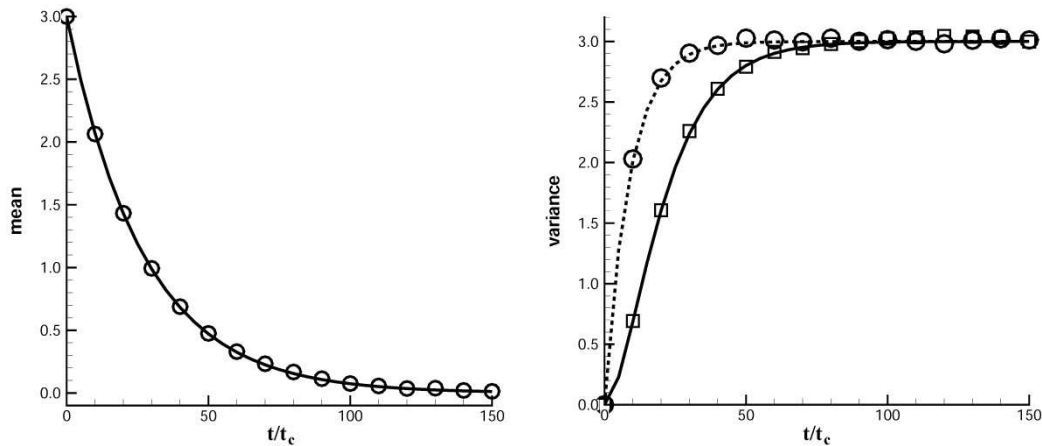


Figure 9: Left: Evolution of the mean value of the electron velocity in x -direction; open symbols: numerical result, full line: exact solution (Eq. (2.12)). Right: Behavior of the electron variances in the course of time for (e,h) collisions. $\sigma_x^2(t)$: simulation result (open squares) and exact solution (full line); $\sigma_y^2(t)$: numerical result (open circles) and analytical solution (dashed line).

a slower dynamics with respect to y (and z not plotted there) due to the initial non-zero group velocity. Probably the most interesting conclusion is drawn from the shape of the electron velocity distribution functions depicted in Fig. 10 (left) which are recorded at time $t/t_c = 200$, that is when steady-state is obviously reached. Unlike the (e,e) collision case in which the velocities were Gaussian distributed around their initial mean values, here they are virtually uniformly distributed around the zero mean value. The visible discrepancy at the left and right edges may be a hint that the longitudinal part of the diffusion (2.8) is not completely balanced by the friction (2.7). Nevertheless, since the numerical simulations agree in an amazing fashion with the exact results obtained from the expressions (2.12) and (2.13) as well as provide reasonable shapes of the velocity distribution function, we propose that the approximations for the friction vector and diffusion tensor (2.7) and (2.8), respectively, represents a "natural quasi conservation" model for inter-species collisions in a plasma. A drawback in some respects is that the solution of the eigenvalue problem to compute \mathbb{B} is computational time consuming. In the following an attractive first order weak alternative is presented which, at least, eases this disadvantage. From the physical point of view it is obvious that for scattering of rapid electrons off infinitely massive ions electron momentum and energy must be conserved exactly in each collision event. Furthermore, in this case the crudest approximation ($\bar{v}_h^2/v^2 \ll 1$) for the friction and diffusion introduced previously seems to be appropriate. However, multiplying both sides of (2.11) by $\hat{\mathbf{V}}^T$, one immediately recognizes that the energy conservation is violated due to the friction force. This problem seemed to be a direct consequence of the approximation of the diffusion tensor which excludes longitudinal diffusion i.e., in the direction parallel to the velocity vector. To overcome this insufficiency we propose the following procedure: Since the square root matrix (2.10) is responsible for the ran-

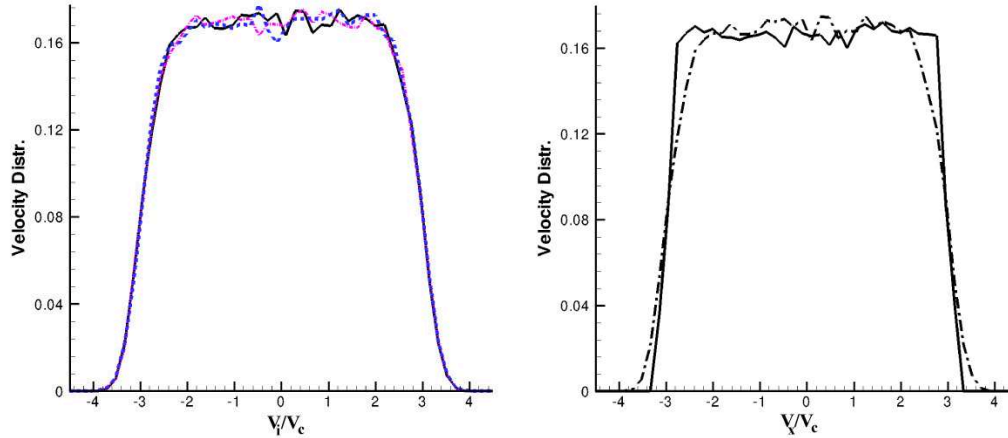


Figure 10: The left plot shows the final electron velocity distribution function of the inter-species collision experiment in dependence of velocity (in all directions), where the friction force and diffusion components are computed from (2.7) and (2.8), respectively. The velocity distribution as a function of v_x (dashed) is compared with this one computed from (4.3) (full line) in the right graph.

domization of the directions, we retain this quantity with its advantageous properties. But instead to drop the friction vector completely (see [10]), we replace α^2 in (2.11) by the yet unknown parameter δ to enforce energy conservation. The electrons are then moved by the time-discretized SDE (2.11) which is given by (see also Eq. (3.5))

$$\mathbf{V}_{n+1} = (1 + \delta \Delta t) |\mathbf{V}_n| \hat{\mathbf{V}}_n + \alpha_n |\mathbf{V}_n| \sqrt{\Delta t} \mathbb{H}_n \vec{\eta}_n, \quad (4.3)$$

where the subscripts indicate the actual time $t = t_n$ and the components of $\vec{\eta}_n$ are Gaussian random numbers with mean zero and variance equal to one. Clearly, δ is then adjusted in such a way that kinetic energy conservation is assured in each collision event. Assuming that $\hat{\mathbf{V}}_n^T \hat{\mathbf{V}}_n = 1$ and neglecting terms in δ^2 , one obtains after some straightforward algebra the result

$$\delta = -\frac{\alpha_n^2}{2} \vec{\eta}_n^T \mathbb{H}_n \vec{\eta}_n. \quad (4.4)$$

The previous electron-ion collision simulation experiment is repeated, where the electrons are now moved according to the Langevin-model (4.3) with (4.4). Additionally, the renormalization method is applied for consistency. The simulation results for the mean value and the variances obtained with this model are nearly identical with those depicted in the Fig. 9. The final electron velocity distribution function for the v_x -component is seen in the right plot of Fig. 10 (full line) together with the result extracted from the left graph (dashed-dotted line) for comparison. It is obvious from this figure that the local enforced energy conservation for each collision event according to (4.3) with (4.4) results in a less smeared velocity distribution at the left and right edges. Moreover, the use of the discretized SDE (4.3) for electron-ion collision modeling reduces the needed CPU time by a factor of ~ 6 compared to this approach, where an eigenvalue problem have to be solved to get the square root tensor \mathbb{B} .

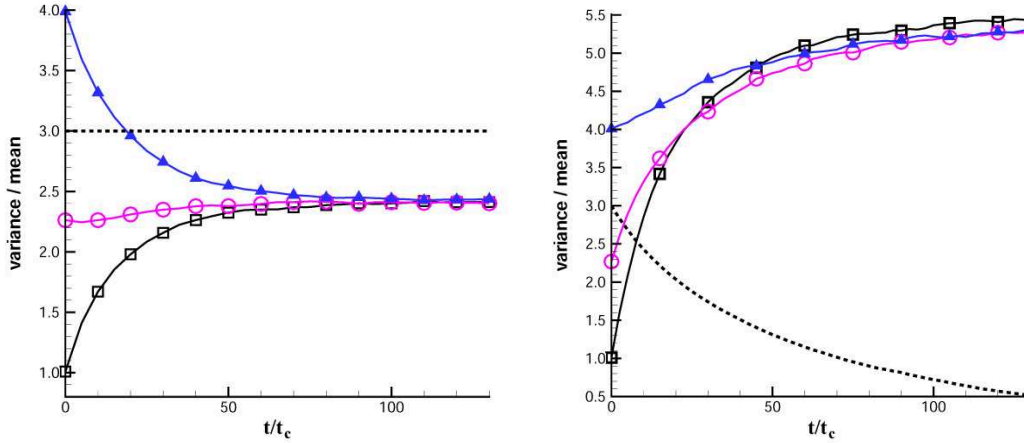


Figure 11: Mean (dashed line) and variance (lines with symbols) time evolution of the three velocity distribution functions during (e,e) collision process (left plot). Here, the mean value remains constant during simulation while the variances tend to a common value. Right plot: Evolution of the mean value and variances during the coupled (e,e)-(e,h) collision process. Thermal energy increases at expenses of the initial kinetic energy in x -direction.

4.3 Coupled calculations: Elastic intra-inter-species scattering

In the following we present results from a more realistic simulation experiment, where both the intra- and inter-species collision modules run together. As in the last sub-section, the ions are thought to be (nearly) immobile with respect to the faster and lighter electrons. The velocities of the latter are initialized with three Gaussians with different variances, respectively,

$$\sigma_x^2(t_0)/v_c^2 = 1.0, \quad \sigma_y^2(t_0)/v_c^2 = 2.25, \quad \sigma_z^2(t_0)/v_c^2 = 4.0,$$

where the electrons impact the ion reservoir with an additional stream velocity $V_x(t_0)/v_c = 3.0$ in the x -direction. For a better understanding of the coupled simulation, we first perform a numerical reference experiment with the described initial data, where the inter-species collisions are switched off. The result of this computation is depicted in Fig. 11 (left). Obviously, the variances reach the equilibrium value

$$[\sigma_x^2(t_0) + \sigma_y^2(t_0) + \sigma_z^2(t_0)] / (3v_c^2) \approx 2.4$$

after ~ 80 time units (which matches to $\sim 17 \mu s$), while the mean value of $\langle V_x \rangle = \mu_x$ stays constant at the initial velocity $V_x(t_0)/v_c = 3.0$ since no randomization mechanism is available to convert the initial kinetic energy into the thermal internal energy; i.e to turn "coherent flow" to "disordered motion". The result of the coupled intra-inter-species simulation is seen in the right plot of Fig. 11. In contrast to the previous experiment, the inter-species collision part provides a mechanism which re-distributes the initial velocities uniformly in each direction resulting in the "decay" of the mean velocity while

the variances (thermal energy) are forced to reach a common value. Consequently, in the coupled numerical experiment the initial kinetic energy is transformed in thermal energy and it is clear from the right plot of Fig. 11 that in this case the variances in each direction will possess a value which is that of intra-species contribution plus one third of the square of the initial flow velocity. Moreover, it is obvious from the right part of Fig. 11 that the coupled calculation is slower than the two independent processes seen in the right and left plots of Figs. 9 and 11, respectively. This observation may be traced back to the fact that the parameter α^2 in Eq. (2.11) is no longer a constant during the simulation. In fact, a comparison of the dashed curve in the right plot in Fig. 11 with that one in Fig. 9 (left) admits the conclusion that α^2 is smaller in the coupled simulation. Although transient non-Gaussian shapes in certain directions may occur due to inter-species collisions, the final result of collisional relaxation is of course a Maxwellian, i.e. a Gaussian distribution function in each direction in velocity space.

5 Conclusion and outlook

In the present paper we have shown that intra-species electron-electron collisions in full velocity space can be effectively modeled using the equivalence between Fokker-Planck (FP) equation and stochastic differential equation (SDE), where the latter equation is solved numerically with explicit weak, up to second order accurate, Itô-Taylor schemes. In conjunction with the computation of the friction force and diffusion on a velocity grid with Fourier techniques at each time step, the proposed Particle-in-Cell- (PIC-) based FP solver allows a fully self-consistent simulation of collisional relaxation. A renormalization method has further been adapted in order to reduce drastically the most of approximation inherent errors, i.e. to ensure the conservation of particles velocity mean and internal energy during the numerical simulations.

The inter-species electron-ion scattering process and some aspects of its numerical modeling have been emphasized in this paper. Due to the natural approximations, the friction and diffusion coefficients are now available in analytical form so that the computations on the velocity grid can be circumvented. Some interesting aspects of the SDE for the randomization of the directions in velocity space related to the lowest order approximation have been found: In this case an analytical solution of both first and second moment can be derived. These results served as natural benchmark to test also the local energy conservation approach for inter-species scattering simulation.

Furthermore, a coupled electron-electron and electron-ion collision simulation has been presented. This numerical experiment gains detailed insight as a non-isotropic initial configuration in velocity space relaxes to a Maxwellian, i.e. a Gaussian distribution function with zero mean and same variances in each direction in velocity space.

Clearly, the presented results of numerical experiments reveal the high quality and reliability of the approximation methods which operate in the Particle-in-Cell-based Fokker-Planck module.

An inherent difficulty of the existing FP solver is closely related with one of the major problems that affects the solution of particle codes, namely, the statistical noise linked with relative low number of particles. Conceivable remedies in this context are the velocity distribution function averaging over several spatial grid cells or the particle creation and destruction technique. Moreover, additional investigations are desirable to decide whether strong numerical approximations of the SDE are also suitable to model intra- and inter-species collisions. However, the main focus for scientific future activities will be the coupling of the FP with a fully electromagnetic Maxwell-Vlasov PIC module, which should bring deeper insight in and better understanding of the complex interaction of collective plasma phenomena with charged particle Coulomb collisions.

Acknowledgments

We gratefully acknowledge the Landesstiftung Baden-Württemberg who funded the development within the program "Modeling and Simulation on High Performance Computers" from 2003–2005 and the Deutsche Forschungsgemeinschaft (DFG) for funding within the project "Numerische Modellierung und Simulation hochverdünnter Plasmaströmungen". D. D'Andrea wishes to thank the Forschungszentrum Karlsruhe for the financial support during the year 2007.

A Aspects of particle-mesh coupling

The shape of the distribution function must be reconstructed on a velocity grid in order to evaluate the integrals (2.5). For this purpose we use a Cartesian mesh in velocity space with an equidistant spacing Δv_1 , Δv_2 and Δv_3 in x -, y -, and z -direction, respectively. The velocity grid vector $\mathbf{v}_{i,j,k} = (v_1(i), v_2(j), v_3(k))^T$ is then given by

$$\mathbf{v}_{i,j,k} = \mathbf{v}_0 + \Delta \mathbf{v}_{i,j,k}, \quad (\text{A.1})$$

where $\mathbf{v}_0 = (v_{01}, v_{02}, v_{03})^T$ is the starting point of the velocity mesh and the increment $\Delta \mathbf{v}_{i,j,k}$ is evaluated according to $\Delta \mathbf{v}_{i,j,k} = (i\Delta v_1, j\Delta v_2, k\Delta v_3)^T$ with $0 \leq i \leq I$, $0 \leq j \leq J$ and $0 \leq k \leq K$.

Reconstruction Block. This step takes place in two distinct phases: first the velocity of particle " ν " is localized with respect to the velocity grid, which means to find out the cell $Z_{i,j,k}$ of the velocity grid where it is met. This grid cell is identified by the indices

$$i_\kappa = \text{INT} \left[\frac{V_\kappa^{(\nu)} - v_{0\kappa}}{\Delta v_\kappa} \right] + 1; \quad \kappa = 1, 2, 3, \quad (\text{A.2})$$

where $\mathbf{V}^{(\nu)} = (V_1^{(\nu)}, V_2^{(\nu)}, V_3^{(\nu)})^T$ is the velocity vector of the ν^{th} particle at time t_n and $\text{INT}(\cdot)$ denotes the integer part of a real number. Note, that the high efficiency of this approach is due to the equidistant grid spacing.

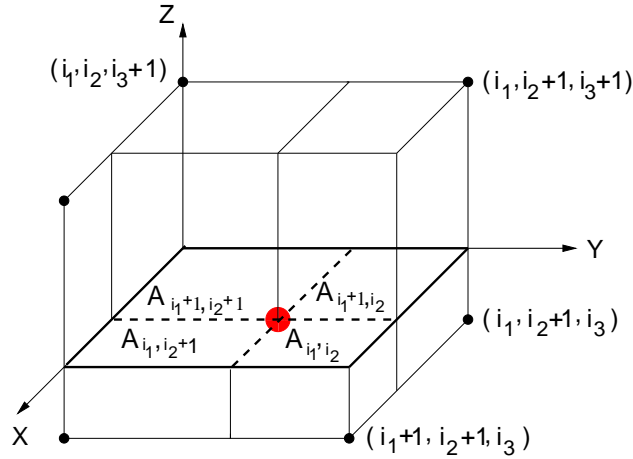


Figure 12: Assignment of the particle's velocity to the nodes (grid-based model) and interpolation of the results obtained in the nodes onto the particle's position in velocity space (mesh-free model) with the aid of the volume-weighting approach.

Second, the contribution of the located particle to the value of the distribution function in each node of grid cell Z_{i_1, i_2, i_3} must be calculated. The basic idea is to take into account the distance of the particle from the node. For this purpose, we apply the concept of assignment functions [24] which are nothing else than B-splines. For sake of clearness we describe this procedure in one dimension. A basic property of a k^{th} order B-spline is that it can be determined recursively [34], for instance, a first order B-spline — in which we are interested here — is computed from the “top-hat” function

$$B_{[i, i+1]}^{[0]}(\xi) := B_{[\xi_i, \xi_{i+1}]}^{[0]}(\xi) = \begin{cases} 1, & \xi \in [\xi_i, \xi_{i+1}), \\ 0, & \text{otherwise,} \end{cases} \quad (\text{A.3})$$

according to

$$B_{[i-1, i, i+1]}^{[1]}(\xi) := B_{[\xi_{i-1}, \xi_i, \xi_{i+1}]}^{[1]}(\xi) = \frac{\xi - \xi_{i-1}}{\xi_i - \xi_{i-1}} B_{[i-1, i]}^{[0]}(\xi) + \frac{\xi_{i+1} - \xi}{\xi_{i+1} - \xi_i} B_{[i, i+1]}^{[0]}(\xi), \quad (\text{A.4})$$

that is the “triangle” function centered around ξ_i , where ξ_i are the nodes of the discretization. The coefficients of $B_{[i]}^{[0]}(\xi)$ appearing in (A.4) are usually called the weights with which a “unit” quantity located at ξ contributes to the node ξ_i . Clearly, if $\xi \in [\xi_i, \xi_{i+1})$ then

$$w_i = w(\xi_i) = \frac{\xi_{i+1} - \xi}{\xi_{i+1} - \xi_i} \quad (\text{A.5})$$

is the only contribution to ξ_i . An index shift $i \rightarrow i+1$ in (A.4) yields the contribution to the node ξ_{i+1}

$$w_{i+1} = w(\xi_{i+1}) = \frac{\xi - \xi_i}{\xi_{i+1} - \xi_i}. \quad (\text{A.6})$$

From this proceeding we immediately obtain the particle assignment weights by identifying ζ with $V_\kappa^{(v)}$ and the nodes ζ_i by $v_\kappa(i_\kappa)$. This concept is easily extended to two- and three-dimensional situations. In that context, we have to calculate the weights $w_{i_1, i_2, i_3}^{(v)} = w^{(v)}(v_1(i_1), v_2(i_2), v_3(i_3))$ of the considered particle with respect to the eight surrounding nodes of grid cell Z_{i_1, i_2, i_3} (see Fig. 12). Geometrically this means, that we have to evaluate the four areas $A_{i_1, i_2, \dots}, A_{i_1+1, i_2+1}$ of the section parallel to the (x, y) -plane, where the particle is located — this is known as the area-weighting method [24, 35]. These areas form the bases of eight cuboids whose volumes are given by

$$w_{i_1+m_1, i_2+m_2, i_3+m_3}^{(v)} = \prod_{\kappa=1}^3 w(v_\kappa(i_\kappa + m_\kappa)); \quad \forall \kappa: m_\kappa \in \{0, 1\}, \quad (\text{A.7})$$

where $w(v_\kappa(i_\kappa + m_\kappa))$ is computed from (A.5) and (A.6). By construction it is not amazing that

$$\sum_{m_1, m_2, m_3=0}^1 w_{i_1+m_1, i_2+m_2, i_3+m_3}^{(v)} = 1 \quad (\text{A.8})$$

holds and, hence, the weights are fractions of the volume of the actual grid cell Z_{i_1, i_2, i_3} .

Interpolation Block. The inverse operation is now also possible: any information stored on the grid nodes can be brought to the particles. The components of the friction force vector and the diffusion tensor — abbreviated by $R_{i_1, i_2, i_3}(t_n)$ — evaluated at the nodes $\mathbf{v}_{i_1, i_2, i_3}$ of the cell Z_{i_1, i_2, i_3} are assigned to the v^{th} particle according to [24]

$$R^{(v)}(t_n) = \sum_{m_1, m_2, m_3=0}^1 w_{i_1+m_1, i_2+m_2, i_3+m_3}^{(v)} R_{i_1+m_1, i_2+m_2, i_3+m_3}(t_n), \quad (\text{A.9})$$

where the weights $w_{i_1, i_2, i_3}^{(v)}$ are already determined in the reconstruction step. The fact that the particle-based weights (A.7) have to be computed only once at the interface mesh-free/grid-based and used for assignment as well as for interpolation is a very attractive feature, which enhances the efficiency of the numerical scheme.

References

- [1] R. Jahn, *Physics of Electric Propulsion*, McGraw-Hill, New York, 1968.
- [2] C. Birdsall, Particle-in-cell charged-particle simulations, plus Monte Carlo collisions with neutral atoms, PIC-MCC, *IEEE Transaction on Plasma Science* 19 (1991) 65–85.
- [3] G. Bird, *Molecular Gas Dynamics and the Direct Simulation of Gas Flows*, Clarendon Press, Oxford, 1994.
- [4] T. Takizuka, H. Abé, A binary collision model for plasma simulation with a particle code, *J. Compt. Phys.* 25 (1997) 205–219.
- [5] S. Ma, R. D. Sydora, J. D. Dawson, Binary collision model in gyrokinetic simulation plasmas, *Computer Physics Communications* 77 (1993) 190–206.

- [6] W. X. Wang, M. Okamoto, N. Nakajima, S. Murakami, Vector implementation of nonlinear Monte Carlo Coulomb collisions, *J. Comput. Phys.* 128 (1996) 209–222.
- [7] K. Nanbu, Theory of cumulative small-angle collisions in plasmas, *Phys. Rev. E* 55(4) (1997) 4642–4652.
- [8] A. V. Bobylev, K. Nanbu, Theory of collision algorithms for gases and plasmas based on the Boltzmann equation and Landau-Fokker-Planck equation, *Phys. Rev. E* 61 (2000) 4576–4586.
- [9] M. Jones, D. Lemons, R. Mason, V. Thomas, D. Winske, A grid-based Coulomb collision model for PIC codes, *J. Comput. Phys.* 123 (1996) 169–181.
- [10] W. Manheimer, M. Lampe, G. Joyce, Langevin representation of Coulomb collisions in PIC simulations, *J. Comput. Phys.* 138 (1997) 563–584.
- [11] M. Rosenbluth, W. MacDonald, D. Judd, Fokker-Planck equation for an inverse-square force, *Phys. Rev.* 107 (1957) 1–6.
- [12] D. Montgomery, D. Tidman, *Plasma Kinetic Theory*, McGraw-Hill, New York, 1964.
- [13] M. Mitchner, C. Kruger, *Partially Ionized Gases*, Wiley, New York, 1973.
- [14] I. Shkarofsky, T. Johnston, M. Bachynski, *The Particle Kinetics of Plasmas*, Addison-Wesley, Reading, 1966.
- [15] R. Hazeltine, J. Meiss, *Plasma Confinement*, Addison-Wesley, Redwood City, CA, 1991.
- [16] C. W. Gardiner, *Handbook of Stochastic Methods*, Springer Verlag, Berlin, Heidelberg, New York, 1985.
- [17] P. Kloeden, E. Platen, *Numerical Solution of Stochastic Differential Equations*, Springer-Verlag, Berlin, Heidelberg, New York, 1999.
- [18] S. Chandrasekhar, Stochastic problems in physics and astronomy, *Reviews of Modern Physics* 15 (1943) 1–87.
- [19] D. Diver, *A Plasma Formulary for Physics, Technology, and Astrophysics*, Wiley-VCH Verlag, Berlin, 2001.
- [20] N. Crouseilles, F. Filbet, Numerical approximation of collisional plasmas by high order methods, *J. Comput. Phys.* 201 (2004) 546–572.
- [21] C.-D. Munz, R. Schneider, E. Sonnendrücker, E. Stein, U. Voß, T. Westermann, A finite-volume particle-in-cell method for the numerical treatment of the Maxwell-Lorentz equations on boundary-fitted meshes, *Int. J. Numer. Meth. Engng.* 44 (1999) 461–487.
- [22] B. Trubnikov, Particle interactions in a fully ionized plasma; in *Reviews of Plasma Physics*, M.A. Leontovich (ed.), Consultants Bureau, New York, 1965.
- [23] D. D'Andrea, Modelling of intra- and inter species charged particle collisions for flow simulation in pulsed plasma thrusters, Ph.D. thesis, Fakultät Luft- und Raumfahrttechnik und Geodäsie, Universität Stuttgart, Germany (2008).
- [24] R. Hockney, J. Eastwood, *Computer Simulation using Particles*, McGraw-Hill, New York, 1981.
- [25] C. Birdsall, A. Langdon, *Plasma Physics via Computer Simulation*, Adam Hilger, Bristol, Philadelphia, New York, 1991.
- [26] B. Albright, D. Winske, D. Lemons, W. Daughton, M. Jones, Quite simulation of Coulomb collision, *IEEE Trans. Plasma Sci.* 31 (2003) 19–24.
- [27] E. Brigham, *The Fast Fourier Transform and its Application*, Prentice-Hall, Englewood Cliffs, 1988.
- [28] W. H. Press, B. P. Flannery, S. A. Teukolsky, W. T. Vetterling, *Numerical Recipes*, Cambridge University Press, Cambridge, 1987.
- [29] B. Oksendal, *Stochastic Differential Equations — An Introduction with Applications*, Springer-Verlag, Berlin Heidelberg, 2000.

- [30] R. Cao, S. Pope, Numerical integration of stochastic differential equations: Weak second-order mid-point scheme for application in the composition PDF method, *J. Comput. Phys.* 185 (2003) 194–212.
- [31] A. Spirkin, A. Gatsonis, Unstructured 3D PIC simulations of the flow in a retarding potential analyzer, *Computer Physics Communications* 164 (2004) 383–389.
- [32] D. Lemons, J. Lackman, M. Jones, D. Winske, Noise-induced instability in self-consistent Monte Carlo calculations, *Physical Review E* 52 (1995) 6855–6861.
- [33] G. Jacobs, J. Hesthaven, G. Lapenta, Simulations of the Weibel instability with a high-order discontinuous Galerkin Particle-In-Cell solver, *44th AIAA Aerospace Sciences Meeting and Exhibit* (2006).
- [34] C. de Boor, *A Practical Guide to Splines*, Applied Mathematical Sciences, Vol. 27, Springer, New York, Heidelberg, Berlin, 1978.
- [35] R. Morse, C. Nielson, Numerical simulation of the Weibel instability in one and two dimensions, *Physics of Fluids* 14 (1971) 830–840.